Multimode Nonlinear Dynamics of Graphene Resonators

Ata Keşkekler,[1,*] Vincent Bos,[1] Alejandro M. Aragón,[1] Farbod Alijani,[1,†] and Peter G. Steeneken[1,2]

[1] *Faculty of Mechanical, Maritime and Materials Engineering, Delft University of Technology, Mekelweg 2, 2628 CD Delft, The Netherlands*

[2] *Kavli Institute of Nanoscience, TU Delft, The Netherlands*

(Received 21 April 2023; revised 2 October 2023; accepted 16 November 2023; published 12 December 2023)

Mechanical nonlinearities dominate the motion of nanoresonators already at relatively small oscillation amplitudes. Although single and coupled two-degree-of-freedom models have been used to account for experimentally observed nonlinear effects, it is shown that these models quickly deviate from experimental findings when multiple modes influence the nonlinear response. Here, we present a nonlinear reduced-order modeling methodology based on finite-element method simulations for capturing the global nonlinear dynamics of nanomechanical resonators. Our physics-based approach obtains the quadratic and cubic nonlinearities of resonators over a wide frequency range that spans 70 MHz. To qualitatively validate our approach, we perform experiments on a graphene nanodrum driven optothermally and show that the model can replicate diverse ranges of nonlinear phenomena, including multistability, parametric resonance, and different internal resonances without considering any empirical nonlinear fitting parameters. By providing a direct link between microscopic geometry, material parameters, and nonlinear dynamic response, we clarify the physical significance of nonlinear parameters that are obtained from fitting the dynamics of nanomechanical systems, and provide a route for designing devices with desired nonlinear behavior.

DOI: 10.1103/PhysRevApplied.20.064020

I. INTRODUCTION

Nanomechanical resonators are the devices of choice for high-performance sensing since they respond to minuscule forces [1–3]. More recently, they have emerged as ideal systems for exploring nonlinear dynamic phenomena. Thanks to their high force sensitivity they are easily driven into the nonlinear regime [4]. Their small mass leads to high resonance frequencies, which facilitates high-speed measurements and, especially in ultrathin resonators, the high aspect ratio allows tuning of tension and resonance frequencies to explore a variety of nonlinear phenomena [5].

When nanomechanical devices are driven into resonance, already at small amplitudes Duffing nonlinearities precipitate in the motion, leading to softening- or hardening-type nonlinear responses [6]. When the nonlinear regime is traversed further, with the increase in drive amplitude, other eigenmodes begin to partake in the motion through autoparametric excitations and nonlinear intermodal couplings [7]. In this nonlinear domain, many studies have reported significant impact of these nonlinear couplings on the effective dissipation and stiffness of the vibration modes [8,9]. A number of exotic nonlinear phenomena that can be used in various applications have also been showcased, ranging from frequency noise suppression [10] and intermodal storage of mechanical energy [11,12], to the generation of mechanical frequency combs [13,14].

Efforts made to date in explaining nonlinear phenomena often rely on proposing analytical nonlinear low-degree-of-freedom (low-DOF) models that are fit to the experimental data to prove their validity. However, since there is no direct link between the magnitude of the resulting fit parameters and the geometry or material properties of the nanomechanical device, it is difficult to evaluate whether these models are the only ones that can account for the experimental data, and which parameters are the most relevant. Moreover, since there is no direct link between the model parameters and the underlying physics, it is difficult to extract device information from the fitting. A realistic description of the complex nonlinear dynamics of nanoresonators with pure analytical methods such as rotating-wave approximation [15] or harmonic balancing [16] is not always sufficiently accurate, because analytical methods are constrained to a limited number of DOFs. Purely numerical methods such as molecular dynamics or dynamic nonlinear finite-element method (FEM) simulations may resolve this issue, yet they are computationally

*a.keskekler-1@tudelft.nl
†f.alijani@tudelft.nl

expensive [17,18] and provide less insight. Therefore, an intermediate approach, whereby analytical multimode nonlinear dynamic models are constructed from the physical device properties using numerical methods, may be extremely valuable for the precise and fast analysis of the nonlinear dynamics of nanomechanical systems.

In this paper we develop and utilize a physics-based reduced-order model (ROM) to characterize multimode nonlinear dynamics of nanomechanical resonators over a wide frequency range. Our approach makes use of FEM simulations to probe the geometric nonlinearities of nanoresonators for a large number of coupled vibrational modes. To validate our method, we perform experiments on a graphene nanodrum that is driven optothermally into the strong mode coupling regime. We show that the physics-based model can capture the response of the seven directly excited and two parametrically excited modes of the graphene nanodrum from linear to nonlinear regime, in a frequency range that spans 70 MHz. The model uses the Young's modulus and prestress to obtain the coupling coefficients, thus providing insight into the influence of geometric and physical parameters on the coupled dynamics of nanomechanical resonators. Since the method is FEM-based, it can be applied further to nanomechanical devices of virtually any geometry, allowing predicting and designing a variety of nonlinear phenomena.

II. RESULTS

A. Nonlinear frequency response measurements

As an experimental model system for demonstrating the method, we probe the complex dynamics of a graphene nanodrum resonator. The resonator is fabricated by dry transfer of $h = 10$-nm-thick multilayer graphene over a $d = 5$-μm-diameter and 285-nm-deep circular cavity, etched in a layer of SiO_2 on a Si substrate. To study the mechanical vibrations of the nanodrum, we optothermally drive it using a blue laser ($\lambda = 405$ nm) and measure its response by a red laser ($\lambda = 633$ nm) using laser interferometry [Fig. 1(a)]. To apply different drive levels to the resonator, we tune only the modulation intensity of the blue laser, while keeping the average power of the blue laser constant to avoid increasing the average temperature of the graphene drum. At low drive powers, a linear set of resonance peaks can be obtained, showing the activation of multiple modes of vibration that we can identify easily using FEM simulations. As the drive level is increased, the nanoresonator quickly shows signs of nonlinearity [Fig. 1(b)]. It is possible to observe the well-studied Duffing (hardening-type) nonlinearity in several modes already at relatively small amplitudes (below −6 dBm).

By further increasing the drive level, we notice rapid activation of a plethora of nonlinear dynamic responses. For instance, when the excitation frequency is tuned to twice the resonance frequency of the modes $f_{0,1}$ and $f_{1,1}$, it is possible to detect strong parametric resonances [19]. Since the tension of the nanodrum is directly related to its stiffness, modulation of the tension via optothermal actuation parametrically excites the nanodrum. Consequently, for conditions where the drive is strong enough, period-doubling instabilities emerge, resulting in parametric resonances [19,20]. These resonances can reach high amplitudes and span wide frequency ranges thanks to the Duffing hardening nonlinearity. Especially at drive

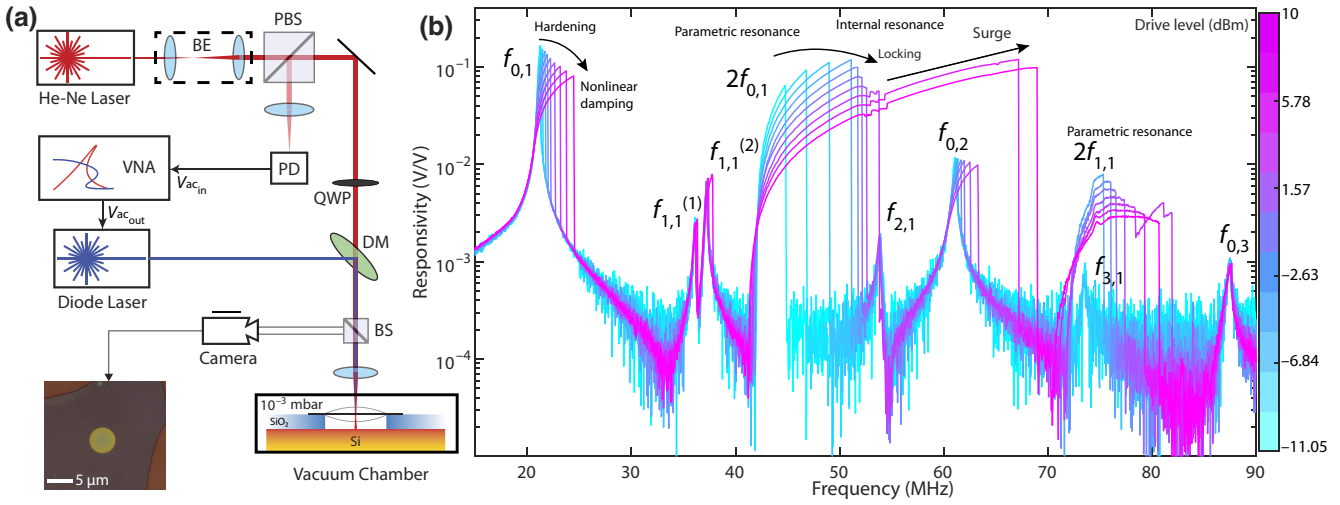

FIG. 1. Measuring the motion of a nonlinear graphene nanodrum. (a) Schematic of the measurement setup. BE, PBS, BS, QWP, DM, and VNA stand for beam expander, polarized beam splitter, beam splitter, quarter-wave plate, dichroic mirror, and vector network analyzer, respectively. (b) Measurements reveal a range of nonlinear dynamic phenomena for the graphene nanodrum at relatively small amplitudes. At high drive levels, the graphene nanodrum exhibits complex nonlinear behavior where the frequency response shows hardening nonlinearity, signatures of nonlinear damping, parametric resonance, mode couplings, and internal resonances. The labels $f_{p,m}$ are frequencies associated with circular drum mode shapes that are found from FEM simulations. Here, p stands for the number of nodal lines and m is the number of nodal circles.

frequencies where the frequencies of these modes satisfy internal resonance conditions [7], they strongly interact with other modes of vibration. This can be observed in Fig. 1(b) at drive levels above 2 dBm, around the region where the parametrically driven $f_{0,1}$ and the directly driven $f_{2,1}$ are interacting. As the parametric response of $f_{0,1}$ approaches $f_{2,1}$, it is also possible to observe a decrease in the responsivity as well as a reduction in the rate of increase in the nonlinear frequency of the parametric resonance—a phenomenon that we label "locking" in Fig. 1(b). Only after a certain drive level is reached is this "locking" barrier surpassed, and the parametric resonance surges to a higher amplitude and frequency [9]. Other than this apparent interaction, a similar coupled dynamic response can be noticed in the neighborhood of the parametrically driven $f_{1,1}$ and directly driven $f_{3,1}$.

Another interesting observation is the decrease in the responsivity of the nanoresonator for the directly driven modes of vibration with the increase in drive level (see the nonlinear response around $f_{0,1}$ and $f_{0,2}$ in Fig. 1(b), for instance). This reduction, which is a result of the emergence of nonlinear dissipation [6], was first observed in resonators that can reach the strong nonlinear regime [21]. It was recently shown that such a nonlinear dissipation process could also be mediated when two modes of vibration are coupled via internal resonance [9]. We note that in scenarios where the drive level is relatively small, these interactions can pertain solely to two modes and the nonlinear oscillations of the resonator can be explained by considering only the two interacting modes and possibly by using solely an analytical model. However, in the experiments we present here, especially at the high drive levels that are being used, modes are activated strongly over wide frequency ranges, like the parametric resonance of the fundamental mode $f_{0,1}$ that spans a frequency range from 40 MHz to 70 MHz and beyond, where modes $f_{2,1}$, $f_{0,2}$ and $f_{3,1}$ reside. Even though it is possible to visually observe the artifacts of modal interactions (like the ones in the proximity of $f_d \approx 55$ MHz and $f_d \approx 80$ MHz), a more subtle sign is the emergence of nonlinear damping induced by these intermodal interactions.

To clarify this further, we note that theoretically, parametric resonances are unbounded in the absence of nonlinear damping. Yet, in our experiments, we observe that the growth of parametric resonance is first bounded by the frequency-locking region at $f_d \approx 2.5 f_{0,1}$ in the vicinity of mode $f_{2,1}$ around 55 MHz. Later, after surpassing the critical drive level (5 dBm), the parametric resonance surges to higher frequencies, yet it still stays bounded, at the vicinity of 68 MHz, just before reaching $f_{3,1}$. This indicates that there is once again a strong source of effective nonlinear damping emerging close to 68 MHz (in addition to the one close to 55 MHz), that is related to the interaction of the fundamental mode with other modes of vibration. Even though it is possible to model the smaller drive level responses in this region (below 5 dBm) using only two modes, it is not possible to replicate the observations at higher drive levels without including an artificial frequency dependent nonlinear damping term, thus suggesting that more modes of vibration will be accounted for in the numerical model. In order to deepen our understanding of these complex multimodal interactions, we thus introduce a FEM-based ROM model [22].

B. Nonlinear reduced-order-modeling procedure

The method for modeling the complex dynamics showcased in Fig. 1(b) consists of five steps, starting with the generation of an FEM model of the nanodevice (step I in Fig. 2). For this purpose, any FEM software package that can handle geometric nonlinearities can be used (we have chosen to use COMSOL in this work). The FEM model of the circular graphene nanodrum resonator uses plate elements and a fixed boundary condition. We use the literature values for the mass density and Poisson's ratio of graphene: $\rho = 2267$ kg m^{-3} and $\nu = 0.16$. As the geometry of the resonator is already known from optical microscopy and atomic force microscopy measurements, this leaves only two unknown parameters to be determined for building the model, namely the pretension and the Young's modulus of the nanodrum. Since the linear resonance frequencies of the graphene membrane are dominated by the pretension, we can extract its value from frequency response measurements at low drive levels. However, if only the fundamental frequency is taken into account when determining the pretension, it is not possible to explain the splitting of the asymmetric modes, like $f_{1,1}^{(1)}$ and $f_{1,1}^{(2)}$ in Fig. 3(a). In a perfectly symmetric drum, these eigenmodes are degenerate, that is, they have the same frequency. But in practice, there is a mismatch in the tension along the in-plane axes that causes these modes to have slightly different frequencies. The frequencies of the first degenerate mode, together with the fundamental frequency, are enough to extract the tension in the membrane by matching the experimental linear resonance frequencies of the first three modes in the FEM analysis. By doing this we found the pretension in the membrane to be $T_x = 0.321$ N m^{-1} and $T_y = 0.257$ N m^{-1} for two perpendicular axes in the plane. To find Young's modulus of the graphene nanodrum we then used the linear resonance frequencies of the higher modes following the method described in [23]; we found a Young's modulus of 410 MPa [Fig. 3(a)], which is within the values reported in the literature [24,25].

By performing linear vibration analysis in the FEM software, we can now obtain the $n \times n$ linear mass and stiffness matrices (**K** and **M**, respectively), as well as the eigenvalues ω_n and eigenmode matrix $\mathbf{\Phi}$, where n is the number of out-of-plane DOFs used in the FEM simulations (step II in Fig. 2). We note that n also corresponds to the number of

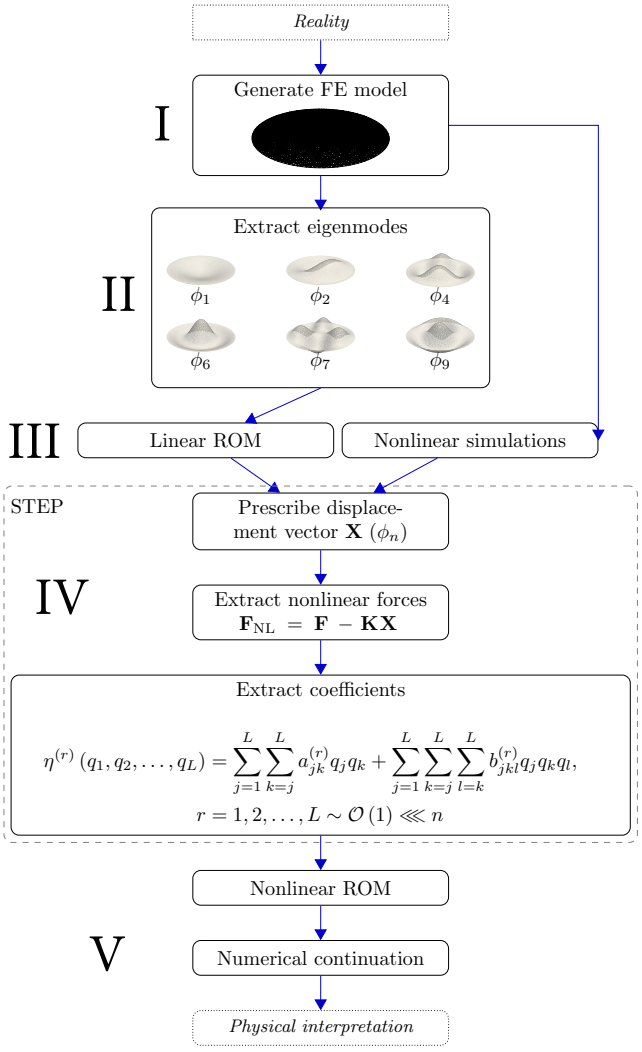

FIG. 2. The flowchart of the ROM procedure for nonlinear dynamic simulations. The frequency response and atomic force microscopy measurements are used to extract the physical parameters for building the finite-element (FE) model, which is then utilized to obtain linear and nonlinear reaction forces of the device, given prescribed displacements in terms of superposition of eigenmodes. These forces are then used for extracting the coefficients of nonlinear terms in the ROM [22]. Finally the nonlinear multimode model is simulated numerically to obtain the full nonlinear dynamic response.

nodes in the simulations, as each node has a single out-of-plane DOF. Therefore, for an n-dimensional displacement vector $\mathbf{X}$ in the FEM model, we obtain the following set of discrete equations:

$$\mathbf{M}\ddot{\mathbf{X}}(t) + \mathbf{C}\dot{\mathbf{X}}(t) + \mathbf{K}\mathbf{X}(t) + \mathbf{H}(\mathbf{X}(t)) = \mathbf{F}(t), \qquad (1)$$

where $\ddot{\mathbf{X}}$ denotes acceleration, $\dot{\mathbf{X}}$ velocity, $\mathbf{H}$ the nonlinear force vector, and $\mathbf{F}(t)$ is the nodal force vector. Here, the linear damping matrix $\mathbf{C}$ accounts for dissipation. Currently nonlinear damping is not yet included in the equation of motion, although viscous material damping might be added via an imaginary term in the material's Young modulus. Evidently, in a finely meshed FEM model, the large number of DOFs n in Eq. (1), in combination with the wide frequency range, makes it practically impossible to use the FEM for simulating nonlinear dynamic responses like those in Fig. 1(b). Therefore, we use a subset L of the n eigenmodes to explain the observed physics, where $L \ll n$. This mathematically means reducing the number of DOFs to only a few that are capable of replicating the nonlinear dynamics of the full model. To do so, we use the modal coordinate transformation $\mathbf{X} = \mathbf{\Phi q}$, expressing the displacement as a superposition of eigenmode shapes, and only select a subset $\mathbf{\Phi}_{n\times L}$ of eigenvectors, such that $\mathbf{q}$ is the L-dimensional modal amplitude vector. Using this transformation, Eq. (1) can be rewritten in modal coordinates as

$$\tilde{\mathbf{M}}\ddot{\mathbf{q}}(t) + \tilde{\mathbf{C}}\dot{\mathbf{q}}(t) + \tilde{\mathbf{K}}\mathbf{q}(t) + \boldsymbol{\eta}(\mathbf{q}(t)) = \tilde{\mathbf{F}}(t), \qquad (2)$$

where $\tilde{\mathbf{M}} = \mathbf{\Phi}^T\mathbf{M}\mathbf{\Phi}$, $\tilde{\mathbf{C}} = \mathbf{\Phi}^T\mathbf{C}\mathbf{\Phi}$, $\tilde{\mathbf{K}} = \mathbf{\Phi}^T\mathbf{K}\mathbf{\Phi}$, $\boldsymbol{\eta} = \mathbf{\Phi}^T\mathbf{H}$ and $\tilde{\mathbf{F}}(t) = \mathbf{\Phi}^T\mathbf{F}(t)$.

From the linear FEM eigenmode simulation, all these matrices and vectors except $\boldsymbol{\eta}$ can be determined (steps I–III in Fig. 2). To obtain this nonlinear matrix we perform multiple nonlinear stationary FEM simulations, with suitably chosen displacements $\mathbf{X}_c$ along the stiffness evaluation procedure (STEP, see IV in Fig. 2) that we briefly outline in what follows and along the lines of Ref. [22].

For any nodal displacement vector $\mathbf{X} = \mathbf{X}_c$, the reaction forces can be transformed into the modal domain and used for the extraction of nonlinear internal forces of the nanodrum. We do this by carefully prescribing nodal displacement vectors $\mathbf{X}_c$ to calculate the corresponding linear reaction forces $\mathbf{F}_L$, since $\mathbf{F}_L = \mathbf{KX}_c$. After finding the linear reaction forces, we perform a full nonlinear static analysis in the FEM package, considering that the nanodrum is subjected to the same displacement vector $\mathbf{X}_c$, and obtain the total nodal reaction force $\mathbf{F}_T$. By subtracting the linear reaction forces from this full static solution, $\mathbf{F}_{\mathrm{NL}} = \mathbf{H}(\mathbf{X}_c) = \mathbf{F}_T(\mathbf{X}_c) - \mathbf{KX}_c$, we then obtain the nonlinear reaction force and map that on the subset of eigenmodes selected as follows: $\boldsymbol{\eta} = \tilde{\mathbf{F}}_{\mathrm{NL}} = \mathbf{\Phi}^T\mathbf{F}_{\mathrm{NL}}$ (see steps III and IV in Fig. 2). We finally expand this nonlinear reaction force for every mode of vibration in terms of quadratic and cubic nonlinear terms as follows:

$$\eta^{(r)} = \sum_{j=1}^{L}\sum_{k=j}^{L} \alpha_{jk}^{(r)} q_j q_k + \sum_{j=1}^{L}\sum_{k=j}^{L}\sum_{l=k}^{L} b_{jkl}^{(r)} q_j q_k q_l, \qquad (3)$$

where r stands for the rth equation of motion also associated with the rth mode, and j, k, l are the mode numbers. Furthermore, L is the number of modes being considered in the ROM. We note that these cubic and quadratic nonlinear terms for single- or two-mode models are commonly

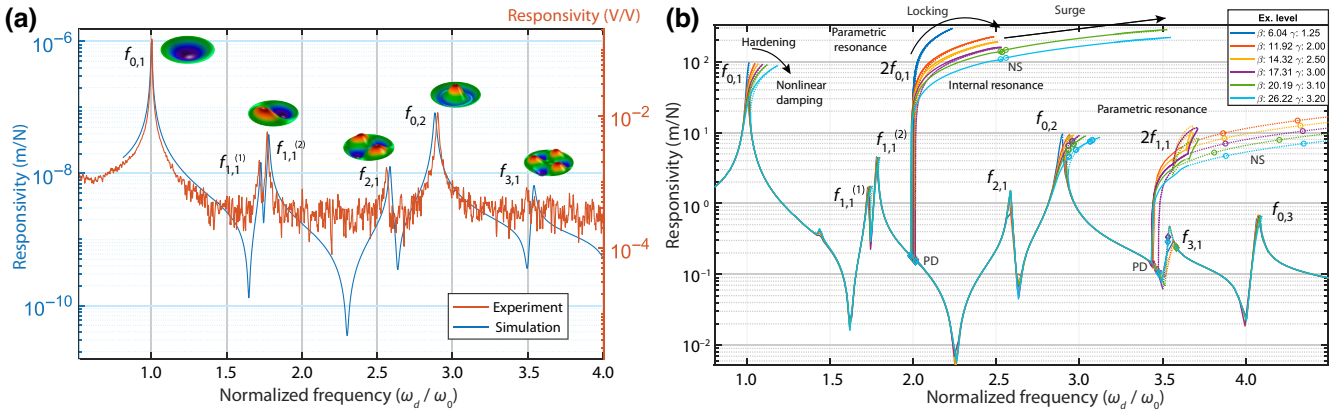

FIG. 3. The simulated linear and nonlinear dynamic responses of the ROM. (a) Frequency response measurements at linear regime are used for extracting the pretension and Young's modulus of the membrane. (b) The simulated nonlinear frequency response of the graphene nanodrum, where β is the direct drive intensity and γ is the parametric drive intensity. It is possible to capture the experimentally observed nonlinear phenomena using the ROM, such as hardening nonlinearities, parametric resonances, and internal resonance-induced physics such as frequency locking and amplitude surge. Bifurcation points are also detected during numerical simulations. Diamond indicators stand for period-doubling bifurcations (PD), whereas circles stand for the Neimark-Sacker bifurcation (NS).

used to simulate nonlinear dynamics of nanomechanical resonators. However, here we extract them purely from geometric nonlinearities and can expand that to any number of modes of vibration, up to the number of DOFs being considered in the FEM simulations.

The procedure explained above enables us to generate a set of linearly independent F_{NL} equations by applying different displacement vectors $\mathbf{X}_c(\phi_r)$, $r = \{1, \ldots, L\}$; these are selected such that they are superpositions of eigenvectors ϕ_r where each combination provides unique information about a nonlinear term through simulations (e.g., $X_c = \pm\boldsymbol{\phi}_j q_j \pm \boldsymbol{\phi}_k q_k \pm \boldsymbol{\phi}_l q_l$). In order to obtain information about the nonlinear reaction forces, the modal amplitudes in the displacement vector $\mathbf{X}_c$ should be chosen such that the nanodevice reaches the geometric nonlinear regime.

To clarify the procedure outlined above, we demonstrate how the nonlinear coefficients of the ROM can be derived for two hypothetical generalized coordinates, q_1 and q_2. We start by determining the uncoupled nonlinear coefficients of the system. For the first generalized coordinate q_1, we construct displacement vectors $\mathbf{X}_c$ from $\boldsymbol{\phi}_1$, such that only nonlinear terms associated with q_1 are activated:

$$\mathbf{X}_1 = +\boldsymbol{\phi}_1 q_1, \tag{4}$$

$$\mathbf{X}_2 = -\boldsymbol{\phi}_1 q_1. \tag{5}$$

This results in two equations with two unknowns:

$$\tilde{\mathbf{F}}^{(1)}_{\mathrm{NL}}(\mathbf{X}_1) = \alpha^{(1)}_{11} q_1^2 + b^{(1)}_{111} q_1^3, \tag{6}$$

$$\tilde{\mathbf{F}}^{(1)}_{\mathrm{NL}}(\mathbf{X}_2) = \alpha^{(1)}_{11} q_1^2 - b^{(1)}_{111} q_1^3, \tag{7}$$

which can be solved to obtain $\alpha^{(1)}_{11}$ and $b^{(1)}_{111}$, which are namely the quadratic and cubic uncoupled nonlinear terms for the modal coordinate q_1. Similarly, by prescribing the system to move on its second eigenmode $\boldsymbol{\phi}_2$ we can obtain $\alpha^{(2)}_{22}$ and $b^{(2)}_{222}$. Next, in order to determine the coupled terms, we use the superposition of the eigenmodes as follows:

$$\begin{aligned} \mathbf{X}_3 &= +\boldsymbol{\phi}_1 q_1 + \boldsymbol{\phi}_2 q_2, \\ \mathbf{X}_4 &= -\boldsymbol{\phi}_1 q_1 - \boldsymbol{\phi}_2 q_2, \\ \mathbf{X}_5 &= +\boldsymbol{\phi}_1 q_1 - \boldsymbol{\phi}_2 q_2, \end{aligned} \tag{8}$$

which results in the following set of three equations with a_{12}, b_{112}, b_{211} as unknowns:

$$\begin{aligned} \tilde{\mathbf{F}}^{(1)}_{\mathrm{NL}}(\mathbf{X}_3) &= \alpha^{(1)}_{11} q_1^2 + b^{(1)}_{111} q_1^3 + \alpha^{(1)}_{12} q_1 q_2 + \alpha^{(1)}_{22} q_2^2 \\ &\quad + b^{(1)}_{112} q_1^2 q_2 + b^{(1)}_{122} q_1 q_2^2 + b^{(1)}_{222} q_2^3, \\ \tilde{\mathbf{F}}^{(1)}_{\mathrm{NL}}(\mathbf{X}_4) &= \alpha^{(1)}_{11} q_1^2 - b^{(1)}_{111} q_1^3 + \alpha^{(1)}_{12} q_1 q_2 + \alpha^{(1)}_{22} q_2^2 \\ &\quad - b^{(1)}_{112} q_1^2 q_2 - b^{(1)}_{122} q_1 q_2^2 - b^{(1)}_{222} q_2^3, \\ \tilde{\mathbf{F}}^{(1)}_{\mathrm{NL}}(\mathbf{X}_5) &= \alpha^{(1)}_{11} q_1^2 + b^{(1)}_{111} q_1^3 - \alpha^{(1)}_{12} q_1 q_2 + \alpha^{(1)}_{22} q_2^2 \\ &\quad - b^{(1)}_{112} q_1^2 q_2 + b^{(1)}_{122} q_1 q_2^2 - b^{(1)}_{222} q_2^3. \end{aligned} \tag{9}$$

Since all of the uncoupled parameters ($\alpha^{(r)}_{jk}$ and $b^{(r)}_{jkl}$ where $j = k = l$) are already known thanks to the previous step, the coupling terms between two modes ($\alpha^{(r)}_{jkl}$ and $b^{(r)}_{jkl}$ where $j = k \neq l$, etc.) can be found by solving these three linearly independent equations [Eq. (9)]. In the case of coupling between three modes of vibration, the third mode's eigenvector will also be included in the prescribed displacement,

TABLE I. Comparison of the nonlinear coupling coefficients for the first two axisymmetric modes of the graphene nanodrum obtained by an analytical method and the ROM approach. Coefficients are normalized by $c = Eh/r^2$ where E is the Young modulus, h is the thickness and r is the radius of the membrane. We note that the quadratic coupling terms are all zero for a flat symmetric membrane.

	Analytic		STEP	
	Mode 1	Mode 2	Mode 1	Mode 2
b_{111}	2.84	−0.57	2.84	−0.57
b_{222}	−3.32	22.76	−3.29	22.9
b_{112}	−1.73	9.25	−1.71	9.27
b_{122}	9.25	−9.96	9.27	−9.85

$\mathbf{X}_c = \boldsymbol{\phi}_j q_j + \boldsymbol{\phi}_k q_k + \boldsymbol{\phi}_l q_l$, and a similar procedure will be followed to obtain $b^{(r)}_{jkl}$, where $j \neq k \neq l$. We note that this procedure can be generalized and easily applied to a system with L modes.

The number of eigenmodes to consider depends on the complexity of the problem and the dynamic range of interest. In our study, and in order to replicate the nonlinear dynamics observed in Fig. 1(b), we used 11 out-of-plane modes in a frequency range that spans 20 MHz to 90 MHz. For convenience, we compare in Table I the coupling terms for the first two axisymmetric modes of an ideal (with uniform tension) nanodrum, obtained analytically [26] (see Sec. I in Supplemental Material [27]) [13] with the finite-element-based ROM approach explained here. We also provide the quadratic and cubic nonlinear terms of the experimentally tested graphene nanodrum for seven modes of vibration in Table 4 in Sec. II of Supplemental Material [27]. As additional examples, we also provide the nonlinear ROM parameters extracted from this protocol for various other nanomechanical systems such as nanomechanical strings and rectangular membrane resonators in Sec. II of Supplemental Material [27].

It is important to mention that the ROM approach sketched here can also account for the influence of in-plane modes of vibration on the nonlinear terms associated with out-of-plane DOFs. This is of great importance for probing nonlinear stiffness terms with accuracy since it has been shown that neglecting the influence of in-plane modes could result in overestimation of the stiffness [16,28]. In the analytical setting, the effects of in-plane modes could be condensed into the out-of-plane modes by assuming zero in-plane inertia since they have frequencies that are orders of magnitude higher, and thus, from the frame of reference of out-of-plane modes, act almost instantaneously. In this way they can be treated statically and their effects can be condensed into the out-of-plane modes, without having to calculate their inertial effects [29]. Instead of including the in-plane modes, the FEM method described here can automatically include their effect more efficiently by leaving the in-plane displacements free (instead of fixed) while applying the out-of-plane membrane displacement $\mathbf{X}_c$. As such, in-plane effects are automatically condensed into the nonlinear parameters out-of-plane modes. After the construction of $\boldsymbol{\eta}$ and the nonlinear ROM, we incorporate the coupled nonlinear differential equations in a numerical continuation package (AUTO) [30] and obtain the steady-state response for different drive frequencies and drive levels, that is, the frequency response (step V in Fig. 2). We utilize the numerical continuation software also to detect bifurcations in the system, which are crucial for understanding the complex nonlinear dynamics of nanoresonators.

C. Simulations of the nonlinear reduced-order-model

We simulate the ROM for different direct and parametric drive levels, $\tilde{F}^{(r)}(t) = F^{(r)}_{\text{dir}} + F^{(r)}_{\text{par}}$, where $F^{(r)}_{\text{dir}} = J^{(r)}\beta\cos(\omega_d t)$ and $F^{(r)}_{\text{par}} = J^{(r)} q_r \gamma \cos(\omega_d t)$, with γ denoting the parametric drive intensity, β the direct drive intensity, and $\mathbf{J}$ the force mapping vector. We shall note that in order to obtain the modal forces $J^{(r)}$, we use the Duffing shift in the frequency of the saddle-node bifurcation of the high-amplitude-solution branches and fit the simulations to the experiments, per drive level. For simplicity, in our simulations we use the Q factor of the fundamental mode ($Q = 180$) for all the modes.

Figure 3(b) shows the simulated frequency response of the nonlinear ROM for various drive levels. Simulations are in good qualitative agreement with the experimental frequency responses in both linear and nonlinear regimes. Although it was attempted to obtain quantitative agreement in the nonlinear regime, this was not fully achieved, possibly due to small imperfections in the membrane that deviate its behavior from the finite-element model. Similarly to experiments, it is possible to observe period-doubling bifurcations of modes $f_{0,1}$ and $f_{1,1}$ around $\omega_d = 2f_{0,1}$ and $\omega_d = 2f_{1,1}$ caused by the parametric drive. When the first parametric resonance reaches the vicinity of the second asymmetric mode $f_{2,1}$, it suffers a reduction in the simulated responsivity in Fig. 3(b) which is consistent with the experimental observation in Fig. 1(b). We also see the frequency locking at the internal resonance. With further increase in the drive level, similarly to the experiments, we observe that the frequency-locking "barrier" is broken, and the frequency of parametric resonance peak surges to 3.5 times the frequency of the fundamental mode $f_{0,1}$. After the surge, we also note the presence of the Neimark-Sacker bifurcation near the internal resonance at $\omega_d/\omega_0 = 2.538$, which indicates the emergence of aperiodic oscillations [13,31].

The experiments and simulations depicted in Figs. 1(b) and 3 demonstrate that, rather than being governed by just two DOFs, the complex motion of the graphene nanodrum around $2.5f_{0,1}$ is a combination of interactions

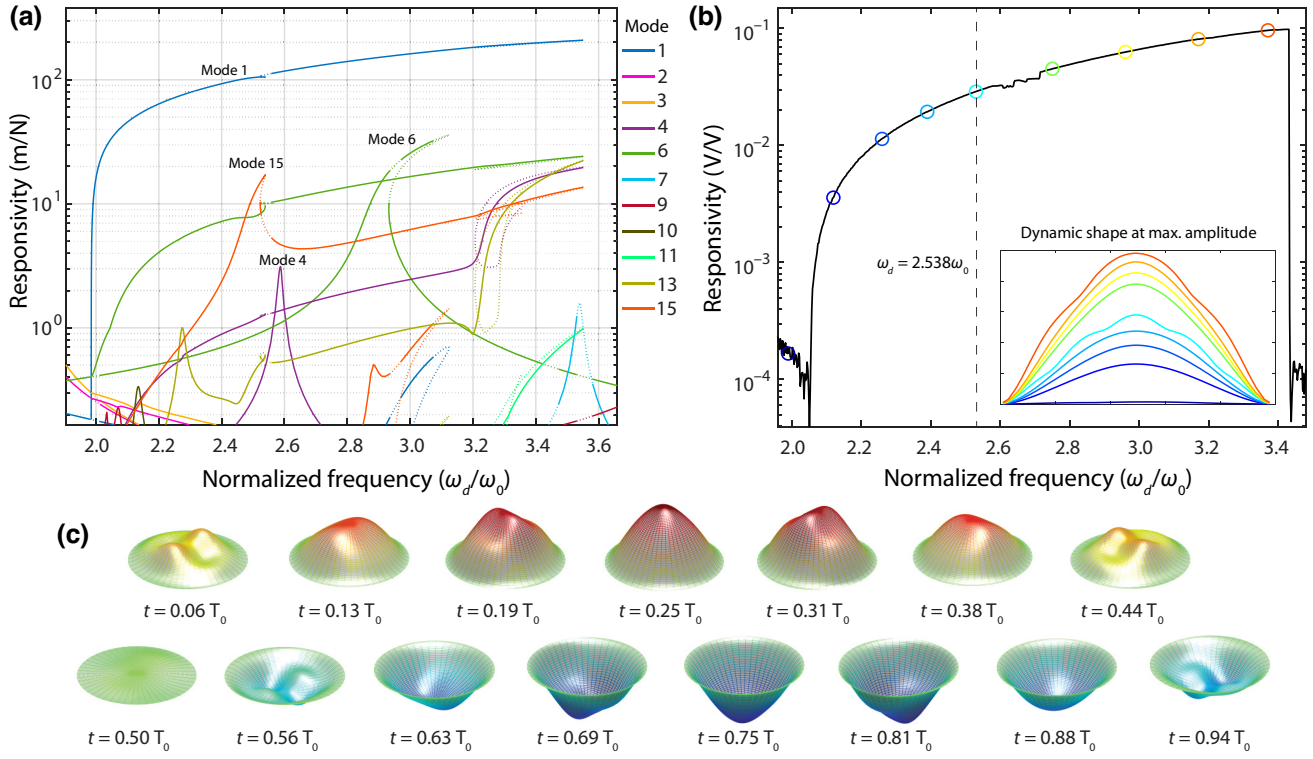

FIG. 4. Simulated overall nonlinear dynamic response of the graphene membrane at principal parametric resonance of $f_{0,1}$. Since modes 5, 8, 12, and 14 are asymmetric modes that are degenerate, they are represented by their degenerate counterparts, modes 4, 7, 11, and 13, respectively. (a) Simulated shape of the membrane at maximum amplitude level during its parametric resonance at specific drive frequencies, displayed on the experimental parametric resonance curve. Solid lines indicate stable solutions, whereas dashed lines indicate unstable ones. (b) Full simulated frequency response at the principal parametric resonance of mode $f_{0,1}$, showing activation of many other modes in the system during the strong parametric resonance, especially around the internal resonance region $\omega_d/\omega_0 = 2.538$. (c) Shape of the membrane during a period of oscillation at internal resonance ($\omega_d/\omega_0 = 2.538$), displaying multiple mode shapes within a single period of oscillation with different frequencies. T_0 is a single period of mode $f_{0,1}$. The amplitude of the response is amplified for visual convenience.

between multiple modes of vibration. We examine the contribution of numerous vibrational modes in the vicinity of the first parametric resonance in order to trace the energy redistribution among various interacting modes. Figure 4(a) shows strong activation of multiple modes at the internal resonance point, where axisymmetric modes $f_{0,2}$ and $f_{0,3}$ (modes 6 and 15) with asymmetric mode $f_{2,1}$ (mode 4) are most notably excited. Time responses of the modes during one period of $f_{0,1}$ oscillation at $\omega_d/\omega_0 = 2.538$ are also shown for convenience (see Sec. III in Supplemental Material [27]). A more visual representation of the time signals can be obtained by using the modal amplitudes q from AUTO to superpose the FEM mode shapes $\boldsymbol{\phi}$, thereby reconstructing the total mechanical response and the deflection shape $\mathbf{X}$ of the graphene nanodrum during internal resonance [see Figs. 4(b) and 4(c)]. If we analyze the nanodrum shape at its maximum amplitude level during an oscillation, we can see that the effective deflection shape is unique near the internal resonance point [Fig. 4(b)]. Dissecting the total motion of the membrane by taking snapshots at different times during a single period of the fundamental mode $f_{0,1}$ [Fig. 4(c)] further reveals the strong influence of the multimodal interaction. It is possible to clearly observe the emergence of other mode shapes during a single oscillation of $f_{0,1}$ parametric resonance. These simulations clearly showcase the energy pathways that lead to the aforementioned nonlinear dissipation phenomenon, not only at the clearly visible internal resonance, but also at responses that look regular, like the direct resonance of $f_{0,1}$. When the global frequency response per mode is analyzed, it is also possible to see the autoparametric activation of multiple modes around $f_{0,1}$ where most of the energy ends up in $f_{0,3}$ (see Sec. III in Supplemental Material [27]).

We note that the favored energy pathways for each system will be distinct due to variations in pretension, geometry, and material properties. These physical parameters dictate the system's capacity to "internally resonate", due to their effects on the nonlinear terms and resonance frequencies. In the literature, it is common to model nonlinear systems by disregarding the effects of multimodal interactions, especially if there are no other visible

modes contributing to the measurement data. Most of the time, as discussed before, this results in using empirical fit parameters to explain the observations. In this case, the assumption is that all the interactions effectively renormalize the terms in the single-mode equation (generally being Duffing or Duffing-van der Pol). The downfall of this assumption is that, in reality, the effects of multimodal interactions are amplitude and drive frequency dependent [9], whereas renormalization through empirical fit parameters assumes constant effects. This means that such simplistic models, at best, will agree with the experiments only for a snapshot of frequency response and cannot explain the overall dynamics at higher drive levels and for wide frequency ranges. Utilizing a method that fully relies on physical parameters and includes as many modes as needed automatically resolves this problem, while clearly displaying the enigmatic nature of these intermodal interactions and energy dissipation pathways.

III. CONCLUSIONS

In summary, we utilized a nonlinear ROM technique to characterize the multimodal interactions of nanomechanical resonators. We used FEM simulations as the basis to develop our physics-based model, which relies purely on measurable quantities from experiments. We calculated the linear and nonlinear internal forces using FEM simulations to extract quadratic and cubic nonlinear terms for constructing the full nonlinear ROM. By simulating the response curves with the model and comparing the results to nonlinear dynamic measurements of a graphene nanodrum resonator, we showed that the model can replicate complex nonlinear intermodal interactions. Moreover, by tracking simultaneous activation of modal amplitudes, we have identified intermodal energy transfer pathways mediated by nonlinear couplings between multiple modes of vibration. Our study provides an efficient and accurate protocol for modeling complex nonlinear dynamics of nanomechanical resonators in a global manner, based purely on material and geometrical parameters. As a result, we anticipate that this protocol will not only aid in explaining the multimode nonlinear dynamics of nanoresonators but also serve as a framework for design optimization of nanoresonators for application purposes [32,33]. Furthermore, our methodology can be directly used to reveal the origins of parasitic effects caused by undesirable nonlinear intermodal interactions [34] and dissipative forces [8,9] that can harm device performance while helping to harness the potent phenomena that nonlinear dynamics can offer [10–14].

[1] J. Chaste, A. Eichler, J. Moser, G. Ceballos, R. Rurali, and A. Bachtold, A nanomechanical mass sensor with yoctogram resolution, Nat. Nanotechnol. **7**, 301 (2012).

[2] F. Fogliano, B. Besga, A. Reigue, L. Mercier de Lépinay, P. Heringlake, C. Gouriou, E. Eyraud, W. Wernsdorfer, B. Pigeau, and O. Arcizet, Ultrasensitive nano-optomechanical force sensor operated at dilution temperatures, Nat. Commun. **12**, 4124 (2021).

[3] I. E. Rosłoń, A. Japaridze, P. G. Steeneken, C. Dekker, and F. Alijani, Probing nanomotion of single bacteria with graphene drums, Nat. Nanotechnol. **17**, 637 (2022).

[4] A. Bachtold, J. Moser, and M. Dykman, Mesoscopic physics of nanomechanical systems, Rev. Mod. Phys. **94**, 045005 (2022).

[5] P. G. Steeneken, R. J. Dolleman, D. Davidovikj, F. Alijani, and H. S. J. van der Zant, Dynamics of 2D material membranes, 2D Mater. **8**, 042001 (2021).

[6] R. Lifshitz and M. C. Cross, in *Reviews of Nonlinear Dynamics and Complexity*, edited by H. G. Schuster (John Wiley & Sons, Weinheim, Germany, 2008), Chap. 1, p. 1.

[7] A. H. Nayfeh and D. T. Mook, *Nonlinear Oscillations*, Wiley Classics Library Vol. 57 (Wiley-VCH, 1995).

[8] J. Güttinger, A. Noury, P. Weber, A. M. Eriksson, C. Lagoin, J. Moser, C. Eichler, A. Wallraff, A. Isacsson, and A. Bachtold, Energy-dependent path of dissipation in nanomechanical resonators, Nat. Nanotechnol. **12**, 631 (2017).

[9] A. Keşkekler, O. Shoshani, M. Lee, H. S. J. van der Zant, P. G. Steeneken, and F. Alijani, Tuning nonlinear damping in graphene nanoresonators by parametric–direct internal resonance, Nat. Commun. **12**, 1099 (2021).

[10] D. Antonio, D. H. Zanette, and D. López, Frequency stabilization in nonlinear micromechanical oscillators, Nat. Commun. **3**, 1 (2012).

[11] M. Wang, D. J. Perez-Morelo, D. Lopez, and V. A. Aksyuk, Persistent nonlinear phase-locking and nonmonotonic energy dissipation in micromechanical resonators, Phys. Rev. X **12**, 041025 (2022).

[12] C. Chen, D. H. Zanette, D. A. Czaplewski, S. Shaw, and D. López, Direct observation of coherent energy transfer in nonlinear micromechanical oscillators, Nat. Commun. **8**, 15523 (2017).

[13] A. Keşkekler, H. Arjmandi-Tash, P. G. Steeneken, and F. Alijani, Symmetry-breaking-induced frequency combs in graphene resonators, Nano Lett. **22**, 6048 (2022).

[14] D. A. Czaplewski, C. Chen, D. Lopez, O. Shoshani, A. M. Eriksson, S. Strachan, and S. W. Shaw, Bifurcation generated mechanical frequency comb, Phys. Rev. Lett. **121**, 244302 (2018).

[15] J. S. Ochs, G. Rastelli, M. Seitner, M. I. Dykman, and E. M. Weig, Resonant nonlinear response of a nanomechanical system with broken symmetry, Phys. Rev. B **104**, 155434 (2021).

[16] D. Davidovikj, F. Alijani, S. J. Cartamil-Bueno, H. S. J. van der Zant, M. Amabili, and P. G. Steeneken, Nonlinear dynamic characterization of two-dimensional materials, Nat. Commun. **8**, 1253 (2017).

[17] D. Midtvedt, A. Croy, A. Isacsson, Z. Qi, and H. S. Park, Fermi-Pasta-Ulam physics with nanomechanical graphene resonators: intrinsic relaxation and thermalization from flexural mode coupling, Phys. Rev. Lett. **112**, 145503 (2014).

[18] B. Sajadi, S. Wahls, S. van Hemert, P. Belardinelli, P. G. Steeneken, and F. Alijani, Nonlinear dynamic identification

of graphene's elastic modulus via reduced order modeling of atomistic simulations, J. Mech. Phys. Solids. **122**, 161 (2019).

[19] R. J. Dolleman, S. Houri, A. Chandrashekar, F. Alijani, H. S. Van Der Zant, and P. G. Steeneken, Opto-thermally excited multimode parametric resonance in graphene membranes, Sci. Rep. **8**, 1 (2018).

[20] Y. Wang, Z. Zhu, Y. Zhang, and L. Huang, Metastable states and energy flow pathway in square graphene resonators, Phys. Rev. E **97**, 012143 (2018).

[21] A. Eichler, J. Moser, J. Chaste, M. Zdrojek, I. Wilson-Rae, and A. Bachtold, Nonlinear damping in mechanical resonators made from carbon nanotubes and graphene, Nat. Nanotechnol. **6**, 339 (2011).

[22] A. A. Muravyov and S. A. Rizzi, Determination of nonlinear stiffness with application to random vibration of geometrically nonlinear structures, Comput. Struct. **81**, 1513 (2003).

[23] B. Sajadi, S. van Hemert, B. Arash, P. Belardinelli, P. G. Steeneken, and F. Alijani, Size- and temperature-dependent bending rigidity of graphene using modal analysis, Carbon **139**, 334 (2018).

[24] A. Castellanos-Gomez, V. Singh, H. S. J. van der Zant, and G. A. Steele, Mechanics of freely-suspended ultrathin layered materials, Ann. Phys. **527**, 27 (2015).

[25] A. Isacsson, A. W. Cummings, L. Colombo, L. Colombo, J. M. Kinaret, and S. Roche, Scaling properties of polycrystalline graphene: a review, 2D Mater. **4**, 012002 (2016).

[26] M. Amabili, Nonlinear Vibrations and Stability of Shells and Plates (Cambridge University Press, Cambridge, 2010).

[27] See Supplemental Material at http://link.aps.org/supplemental/10.1103/PhysRevApplied.20.064020 for the analytical model of an ideal membrane with two degrees of freedom, nonlinear reduced-order model parameters for different nanomechanical resonators, and additional simulation results for dynamic response of the graphene drum during internal resonance.

[28] A. Sarafraz, A. Givois, I. Roslon, H. Liu, H. Brahmi, G. Verbiest, P. G. Steeneken, and F. Alijani, Dynamics of pressurized ultra-thin membranes, arXiv:2212.05464 (2022).

[29] M. P. Mignolet, A. Przekop, S. A. Rizzi, and S. M. Spottswood, A review of indirect/non-intrusive reduced order modeling of nonlinear geometric structures, J Sound Vib. **332**, 2437 (2013).

[30] E. J. Doedel, A. R. Champneys, F. Dercole, T. F. Fairgrieve, Y. A. Kuznetsov, B. Oldeman, R. Paffenroth, B. Sandstede, X. Wang, and C. Zhang, Auto-07p: Continuation and bifurcation software for ordinary differential equations, (2007). https://www.macs.hw.ac.uk/~gabriel/auto07/auto.html.

[31] G. Gobat, V. Zega, P. Fedeli, C. Touzé, and A. Frangi, Frequency combs in a mems resonator featuring 1:2 internal resonance: ab initio reduced order modelling and experimental validation, Nonlinear Dyn. **111**, 2991 (2023).

[32] S. Dou, B. S. Strachan, S. W. Shaw, and J. S. Jensen, Structural optimization for nonlinear dynamic response, Philos. Trans. R. Soc. A: Math., Phys. Eng. Sci. **373**, 20140408 (2015).

[33] L. L. Li, P. M. Polunin, S. Dou, O. Shoshani, B. Scott Strachan, J. S. Jensen, S. W. Shaw, and K. L. Turner, Tailoring the nonlinear response of MEMS resonators using shape optimization, Appl. Phys. Lett. **110**, 081902 (2017).

[34] U. Nabholz, M. Curcic, J. E. Mehner, and P. Degenfeld-Schonburg, in *2019 IEEE International Symposium on Inertial Sensors and Systems (INERTIAL)* (IEEE, 2019), p. 1.